

Xie, Yiting and Padgett, Jennifer and Biancardi, Alberto M. and Reeves, Anthony P. "Automated aorta segmentation in low-dose chest CT images", International Journal of Computer Assisted Radiology and Surgery, 2014, 9(2): 211-219.

doi=10.1007/s11548-013-0924-5,

url=<http://dx.doi.org/10.1007/s11548-013-0924-5>

Downloading of the paper is permitted for personal use only. Systematic or multiple reproduction, duplication of any material in this paper for a fee or for commercial purposes, or modification of the content of the paper are prohibited.

# Automated Aorta Segmentation in Low-dose Chest CT Images

Yiting Xie, Jennifer Padgett, Alberto M. Biancardi, and Anthony P. Reeves

Email: [yx269@cornell.edu](mailto:yx269@cornell.edu), [jjp263@cornell.edu](mailto:jjp263@cornell.edu), [amb284@cornell.edu](mailto:amb284@cornell.edu), [reeves@ece.cornell.edu](mailto:reeves@ece.cornell.edu)

School of Electrical and Computer Engineering

Cornell University

Ithaca, New York

## Abstract

### Purpose.

Abnormalities of aortic surface and aortic diameter can be related to cardiovascular disease and aortic aneurysm. Computer based aortic segmentation and measurement may aid physicians in related disease diagnosis. This paper presents a fully automated algorithm for aorta segmentation in low-dose non-contrast CT images.

### Methods.

The original non-contrast CT scan images as well as their pre-computed Anatomy Label Maps (ALMs) are used to locate the aorta and identify its surface. First a seed point is located inside the aortic lumen. Then a cylindrical model is progressively fitted to the 3D image space to track the aorta centerline. Finally the aortic surface is located based on image intensity information. This algorithm has been trained and tested on 359 low-dose non-contrast CT images from VIA-ELCAP and LIDC public image databases. Twenty images were used for training to obtain the optimal set of parameters while the remaining images were used for testing. The segmentation result has been evaluated both qualitatively and quantitatively. Sixty representative testing images were used to establish a partial ground truth by manual marking on several axial image slices.

### Results.

Compared to ground truth marking, the segmentation result had a mean Dice Similarity Coefficient of 0.933 (maximum 0.963 and minimum 0.907). The average boundary distance between manual segmentation and automatic segmentation was 1.39mm with a maximum of 1.79mm and a minimum of 0.83mm.

### Conclusion.

Both qualitative and quantitative evaluations have shown that the presented algorithm is able to accurately segment the aorta in low-dose non-contrast CT images.

*Keywords—*aorta segmentation; computer based automated segmentation; low-dose non-contrast CT images; anatomy based segmentation

## I. INTRODUCTION

The quantitative measurement of the aortic surface is important for cardiovascular disease diagnosis [1]. It can be accomplished through human inspection by a radiologist or through computer algorithms [2]. We present a fully automated algorithm to segment the aorta in low-dose non-contrast CT scans. This algorithm could be used as the basis for the automated detection of aortic aneurysm. It may also be used to detect other chest diseases and risk factors associated with the aorta.

Automated aorta segmentation has been developed and evaluated on contrast enhanced [3, 4] and non-contrast enhanced [5, 6] CT images as well as MR images [7-9]. In contrast enhanced CT images and MR images, the aorta typically has a well-defined boundary and can be segmented using simple threshold and edge detection methods. However, these methods do not translate well to the low-dose CT images where the edge of the aorta is not well defined. Compared to regular dose CT, low-dose CT exposes subjects to less radiation and is becoming more popular for procedures such as cancer screening [10].

Isgum et. al [6] performed multiple atlas based registrations to segment the aorta in low-dose non-contrast CT images. Multiple manually segmented atlases were mapped onto a target image before a decision fusion rule was used to determine the segmented region in the target image. Their algorithm was tested on 14 low-dose non-contrast CT images and achieved a best mean Jaccard coefficient of 0.78. Kurkure et. al [5] first approximated the aorta location and then used dynamic programming to detect the aortic boundary contour.

Their algorithm was tested on 37 non-contrast CT scans and achieved an average Dice Similarity Coefficient of 0.88 for the ascending aorta and 0.96 for the descending aorta.

We present a novel three-stage aorta segmentation algorithm. In the first stage a seed point inside the aortic lumen is automatically determined. In the second stage the entire aorta is tracked, starting from the seed point, yielding a set of points that represent the aortic centerline. In the third stage, the aortic surface is determined using the centerline and image intensity information. This algorithm builds upon vessel segmentation methods of cylinder tracking developed in previous work [17]. Key contributions of this algorithm that accommodate the high-noise associated with low-dose CT images are: the use of an anatomy labeled map to locate the aortic regions and the use of local neighboring ray filtering to identify the surface location of the aorta.

## II. ALGORITHM

The automated segmentation algorithm makes extensive use of pre-computed Anatomy Label Maps (ALMs) in all stages. Each CT image in the database has an ALM [11], which is a pixel-based partially labeled image with the same geometry and resolution as the original intensity image as shown in Figure 1. In an ALM, pixels that have been identified as belonging to an anatomical entity are given a unique label while all other pixels are marked as unlabeled. Therefore, the spatial locations of pre-identified organs can be directly obtained from the ALM. Figure 1 shows identified organs including lungs, vertebrae, ribs and airways in different colors.

The ALMs are created by a process of successive step-by-step refinements, starting with the most robust region segmentations first. The segmented regions then provide constraints for the segmentation of other unidentified entities. For example, Lee et al [14] described an automated method to segment the trachea and airways using region growing and subsequently in [19] a bone tracing and segmentation algorithm; both have been incorporated into the ALM. For this work, the airway lumens, lung regions, bone structures and significant regions of fat have all been robustly identified in the ALM.

Any mis-labeling in ALMs usually occurs in CT scans with highly abnormal anatomy such as lung resection or major image artifacts resulting from metal implants. For the combined 380 thin slice cases from the VIA-ELCAP and LIDC image database, the ALM failed in 21 cases (5.5%) with mis-labeled trachea or bones. Among these 21 cases, 8 cases contain metal implants and the remaining cases have abnormal anatomy structure. These cases were not considered in this paper.

### A. First Stage - Location of Aorta Center

The first stage locates a seed point to start tracking the aorta centerline. Empirical review indicated that the descending aorta is well defined in the axial image at the level of the carina by its geometry with respect to the anatomy labeled map of the lungs, vertebra and the carina itself. In order to obtain the location of the carina the airways including the trachea are segmented using a cylinder tracking and region-growing algorithm [14]. The carina is the location where the trachea divides into two main bronchi; the axial slice that contains the carina location is selected for analysis. The aortic center is located in that slice by fitting the largest circle into the unlabeled region adjacent to left lung and vertebra in the map.

Figure 1. shows an axial slice of a CT scan with its pre-computed anatomy map. It is observed that descending aorta at the carina level is spatially bounded by the left lung and vertebra. Thus the algorithm searches within the anatomy map and fits the largest circle inside the empty space adjacent to left lung and vertebra.

The center of the chosen circle is the initial seed point. The detected seed point may not be at the exact center of aortic lumen; however, any seed point inside the lumen is sufficient for the cylinder-tracking algorithm.

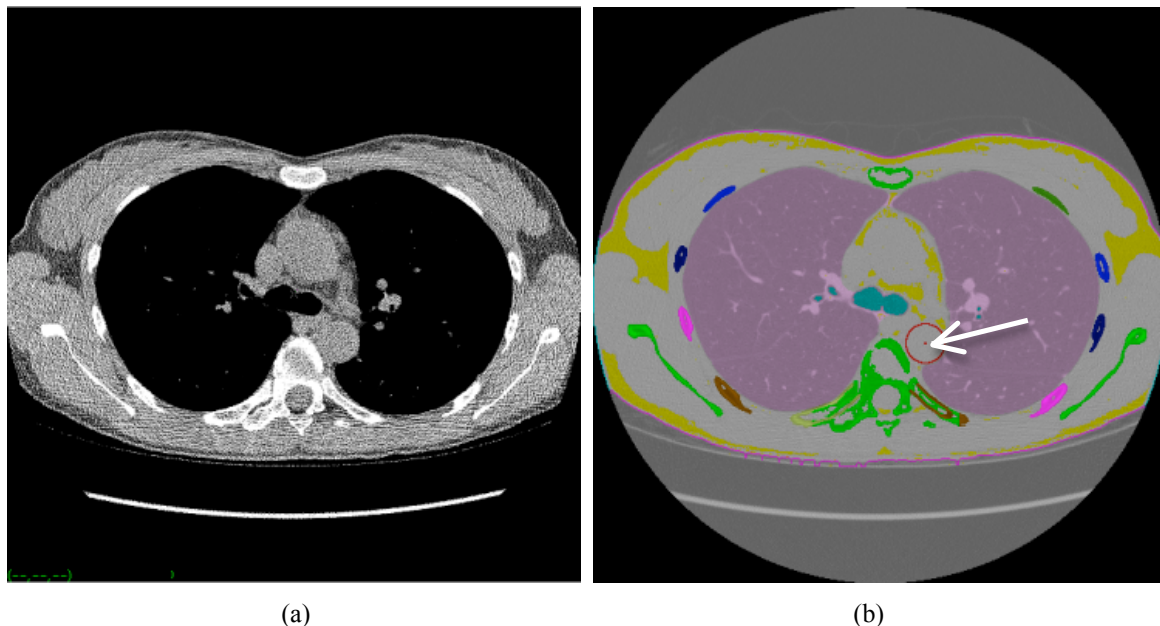


**Fig. 1.** 1(a) original CT scan, 1(b) the corresponding ALM. The largest detected circle and its center which is the algorithm seed point is marked in red and indicated by the arrow. In 1 (b) the lung regions are shown in pink the vertebrae are labeled green, the airways are labeled in blue and fat is labeled in yellow.

### B. Second Stage - Aorta Tracking

The aorta may be approximately modeled as a series of discrete, overlapping cylinders. A cylinder-tracking algorithm is used to track the aorta in upward and downward directions from the seed point. This algorithm is based on a method developed by Fotin et al. [17] for coronary artery segmentation in CTA images. With an initial seed point and direction, cylindrical sections are iteratively fit to the 3D image space defined by unlabeled pixels in the ALM until a termination condition is met. The cylinder tracking is performed in the ALM rather than the original image because the ALM contains well-defined constraining structures that have been robustly identified. The length of candidate cylinder segment depends on the aortic arch curvature and aortic diameter. In upward tracking, a cylinder should be long enough to progress in the correct direction but also be short enough to go through the curved aortic arch. A shorter cylinder also corresponds to a longer tracking time. A range of values from 5 mm to 100 mm was explored and the model cylinder height was chosen to be the most robust value, 20 mm.

The initiation and general progress of cylinder tracking is shown in Figure 2. The upward aorta tracking and segmentation above the carina level is termed superior aorta tracking or segmentation.

Figure 2(b) shows the tracking process. In equation 1,  $S$  is the matching score,  $w_i$  and  $w_j$  are voxels of a candidate cylinder and  $M$  is a weight for any already labeled voxels.  $w_i$  is 0 for unlabeled voxels in the ALM and 1 for labeled voxels.  $M$  is set to penalize candidate cylinders that include already labeled voxels. The goal is to find a cylinder with maximum unlabeled voxels and minimum labeled voxels. The penalty term  $M$  for  $S$  allows a very small number of labeled voxels to be accepted in the candidate cylinder region at a high cost. In this way a small number of ‘noise’ voxels of the ALM that may occur within the aortic region maybe accommodated. Without this term a single inaccurately labeled voxel in the aortic lumen could prevent successful tracking. However, too small a value for  $M$  would result in poor quality tracking. For our training cases we found that a value of 30 for  $M$  was sufficient for good tracking of all cases. The outcome of the

tracking algorithm is the set of center points of all the ‘best’ matching cylinders, which approximate the actual aortic centerline.

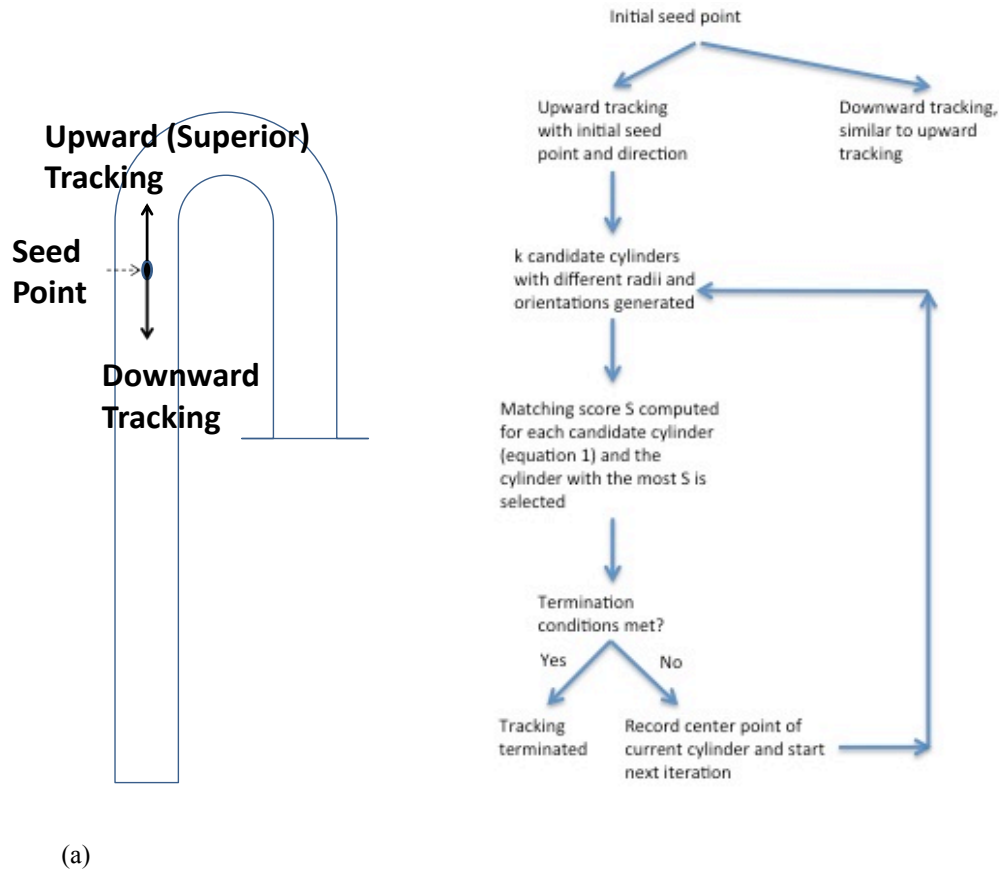


**Fig. 2.** 2(a) shows a cylinder tracking model with a seed point and two initial tracking directions for upward and downward aortic tracking. 2(b) shows the general tracking process.

$$S = \sum_{w_i=0} w_i - M \times \sum_{w_j \neq 0} w_j \quad (1)$$

Figure 3 shows the search space for candidate cylinders in the  $t^{th}$  iteration based on the previous best cylinder. The search for a new cylinder follows these steps:

(1) New cylinder  $x_t$  progresses for length  $\Delta_{step}$  along  $\vec{d}_{t-1}$ , the direction of previous cylinder  $x_{t-1}$ . Both  $x_{t-1}$  and  $x_t$  have height  $h_0$ .  $\Delta_{step}$  is set to  $0.2h_0$ .

(2) New cylinder has radius  $r_t$  and its direction  $\vec{d}_t$  is parameterized by azimuthal angle  $\alpha$  and polar angle  $\beta$ .

The search space for these parameters is given in equation 2-4. The step size used in the search is  $\frac{\pi}{32}$  for both  $\alpha$  and  $\beta$ .

(3) The best new cylinder  $C_t$  is determined by equation 5.

$$r_t \in [0.5 * r_{t-1}, 2 * r_{t-1}] \quad (2)$$

$$\alpha \in [0, 0.2\pi] \quad (3)$$

$$\beta \in [0, 2\pi] \quad (4)$$

$$C_t = \operatorname{argmax}_{\{r, \alpha, \beta\}} \mathcal{S} \quad (5)$$

- (4) Tracking is terminated if the radius of the best matching cylinder changes significantly or if the maximum matching score is below 0, i.e. none of the candidate cylinders has enough unlabeled voxels to be considered as an appropriate match. A significant change occurs when the radius of a new cylinder changes by more than two times or less than a half from any of the previous 10 cylinders.

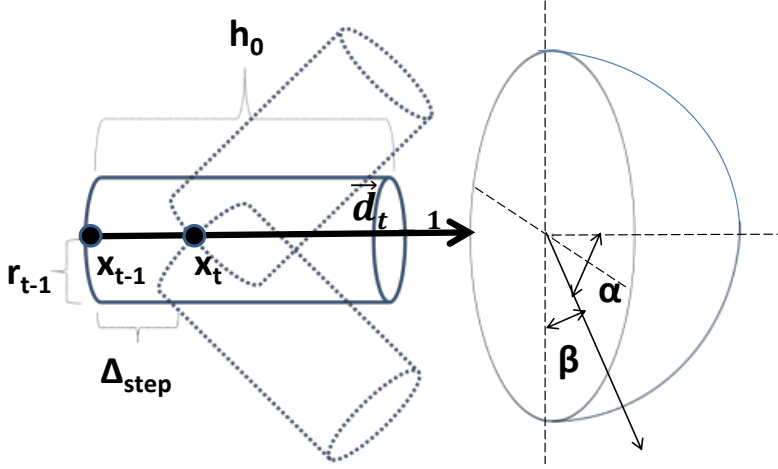


**Fig. 3.** Cylindrical tracking model and parameters [15].

### C. Third Stage - Aortic Surface Refinement

The third stage locates the aortic surface. Given that the general location of the aorta is already constrained by its centerline, the detailed refinement of the aortic surface is constrained in a direction perpendicular to the centerline and in the region of the estimated radius from the best fitting cylinder. Lee et. al [16] proposed a triangular mesh model in airway wall thickness measurement. This was adapted to involve a new surface detection algorithm in order to find the more subtle aortic surface.

The triangular model provides a uniform tessellation of the aortic surface, which is a convenient topology for surface analysis as shown in Figure 4(a). The mesh spacing parameters are set such that when mapped to the surface of the aorta the triangles will have an extent of about 4mm ensuring that they represent more than one surface voxel.

The surface of the aorta is identified as follows:

- (1) The centerline determined in stage 2 is broken into 5 segments with approximately the same length. A third order polynomial is fit to each segment of the centerline.
- (2) A triangular mesh model with unit diameter is mapped to each polynomial centerline segment with an interval between rings along the axis of 4mm. A ring refers to the set of triangles on the same level perpendicular to the centerline (Figure 4(b)).
- (3) Rays are projected perpendicular to the centerline through the center of each triangle in the mesh ( Figure 4(b)).

- (4) Local neighborhoods of rays are evaluated together to detect the aortic surface location for the center of each mesh triangle.
- (5) The triangle mesh projected to the aortic surface is mapped back to the original image space to determine the aorta segmentation.

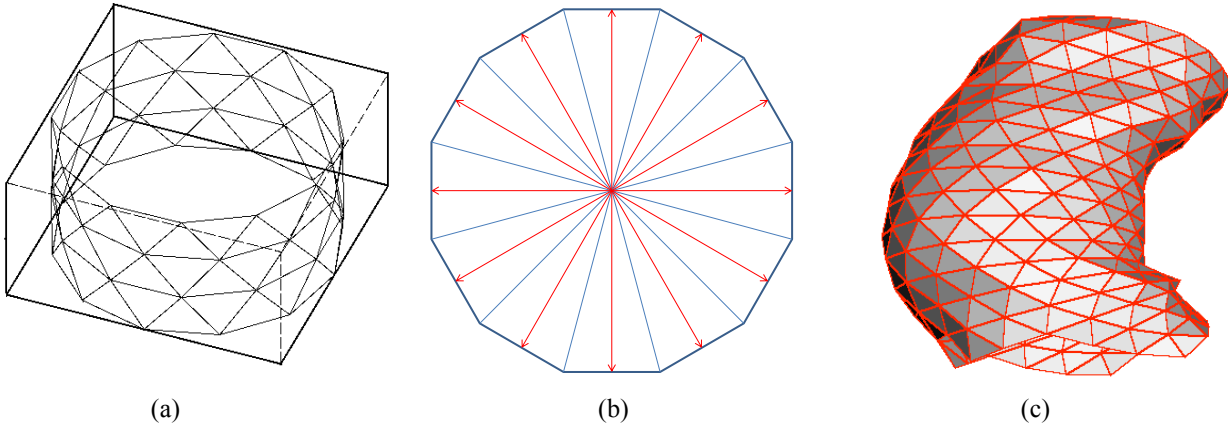


**Fig. 4.** (a) a section of the triangular mesh model. (b) one ring of triangles perpendicular to the centerline. Red lines represent rays. (c) the detected aortic surface represented by the triangular mesh.

Each ray is traced until it intersects with an ALM label or the image intensity falls to -30HU, which is the intensity level for a tissue less dense than the aorta such as fat.

In order to reduce the impact of noise the value for a ray for each location is determined by the mean of its neighbors. That is, smoothing is applied perpendicular to the rays' direction. The following algorithm determines the location of the aortic surface of a ray.  $s_1, s_2, \dots, s_t$  are sample values on an original ray before mean filtering and threshold  $T$  is set to -30HU.

- (1) Intensity values  $s_1, s_2, \dots, s_t$  of ray  $S$  are averaged with its 12 neighboring rays  $N_1$  to  $N_{12}$  to reduce the effect of noise (see Figure 5), producing  $\bar{s}_1, \bar{s}_2, \dots, \bar{s}_t$  as defined in equation 6.
- (2) Starting from  $\bar{s}_1$  to  $\bar{s}_t$ , if  $\bar{s}_i < T$  and  $\bar{s}_{i+1} < T$  and  $\bar{s}_{i-1}$  position is unlabeled in the anatomy map, this ray terminates at  $(i-1)$  position.
- (3) If such termination position cannot be found, the ray terminates at position  $\bar{s}_j$ , where  $\bar{s}_j$  is unlabeled and  $\bar{s}_{j+1}$  is labeled in the anatomy map.
- (4) If a termination point can be found in step 2 or 3, a ray is successfully terminated. If a termination position still cannot be found for a ray  $S$ , the average length of the successfully terminated neighboring rays in the same ring at  $N_6, N_7, N_8$  and  $N_9$  is assigned to be the length of ray  $S$ . This step is post-processing and the incorporation of near neighbors guards against extreme single outliers.

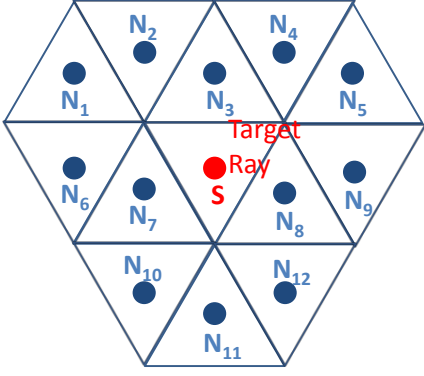


**Fig. 5.** Red dot is the target ray and blue dots represent its 12 neighbors.

$$\{\overline{s_1}, \overline{s_2}, \dots, \overline{s_f}\} = \frac{S + N_1 + N_2 + \dots + N_{12}}{13} \quad (6)$$

### III. EXPERIMENTS

#### A. Data

The segmentation algorithm was trained and evaluated on thin slice (less or equal to 1.25mm) chest CT scans from the VIA-ELCAP public image database [12] and from the LIDC public image database [13].

The VIA-ELCAP image database consists of 50 low-dose non-contrast chest CT images; 20 cases were used for training, 35 cases were used for testing and 5 cases were rejected from the study due to excessive image artifacts caused by metal implants.

The LIDC database contains 335 non-contrast thin slice chest CT images and 314 images were used for evaluating the algorithm while the other 21 cases were rejected from consideration due to implant artifacts (8 cases) and abnormal anatomy structures (13 cases).

#### B. Experiment 1: Qualitative evaluation

The segmentations were rated on quality for all stages of the algorithm. For the final stage a suboptimal result was recorded if the full aorta was not segmented (i.e. the segmented aorta terminated too early) or the surface of the aorta had an error in excess of a nominal 3mm or more by visual inspection. This inspection was performed by reviewing the original image overlaid by the segmentation. The reader was first calibrated by reviewing a number of cases in which the actual error was measured with electronic calipers. Figure 6 shows example images and their maximum boundary error measured with electronic calipers.

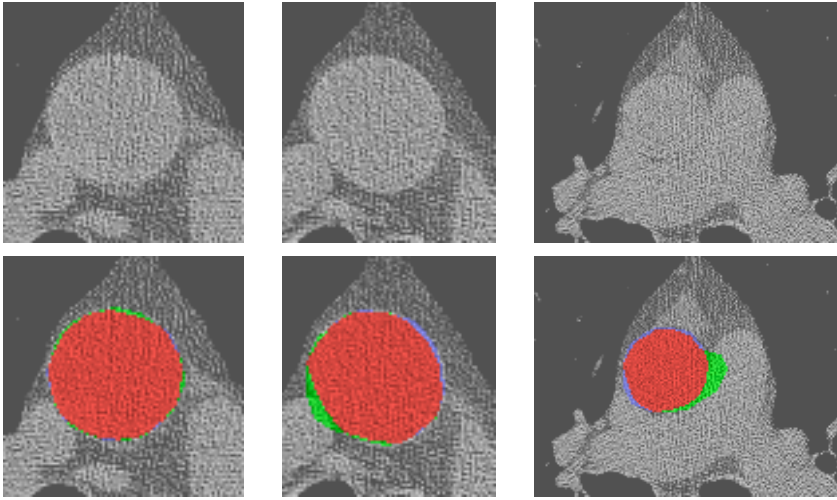


**Fig. 6.** Upper images are original intensity images while corresponding lower images are manually segmented aorta v.s. automatically segmented aorta. Red denotes the overlapping region, green denotes the false positive region and blue denotes the false negative region. Segmentation on the left, middle and right has a maximum boundary error of 1.2mm, 3.1mm and 4.0mm respectively based on electronic caliper measurements.

### C. Experiment 2: Quantitative evaluation

Sixty randomly selected scans from the testing set of the VIA-ELCAP database were sparsely manually marked to evaluate the automated segmentation. Thirty out of the sixty cases have 18 images marked per case: 5 images for ascending aorta, 10 images for descending aorta and 3 images for aortic arch marked in the coronal plane. The other thirty cases have 3 images marked per case: one for ascending, one for descending and one for aortic arch. In total, there are 630 carefully marked images being used for evaluation. The regions enclosed by the manual markings were compared to the automated aorta segmentation for those images.

The quality of the segmentation was characterized by both the Dice Similarity Coefficient (DSC) and a boundary distance measurement. The DSC was used to compare manually segmented region  $S_m$  with automatically segmented region  $S_a$ . The DSC is defined as  $\frac{2|S_m \cap S_a|}{|S_m| + |S_a|}$ , in which 0 is the outcome for no overlap and 1 is the outcome for complete overlap. For each scan used in quantitative evaluation, the DSC is first computed for all marked slices. Then the marked slices are further grouped into ascending slices and descending slices, yielding two results representing the ascending and descending aorta segmentation respectively. For each pair of  $S_m$  and  $S_a$ , number of true positives  $tp$ , number of false positives  $fp$  and number of false negatives  $fn$  are also computed. A true positive pixel exists in both the manually marked and the automatically segmented aorta. A false positive pixel only exists in automated segmentation and a false negative pixel only exists in manual marking.

A bias term  $B_{pn}$  is computed as in equation 7.  $B_{pn}$  compares the values of  $fp$  and  $fn$ . It is scaled as a fraction of the size of the target object, i.e. it denotes the percentage of bias in true positives. If  $B_{pn}$  is greater than 0, the automated algorithm tends to over-segment. If  $B_{pn}$  is less than 0, the algorithm tends to under-segment.

$$B_{pn} = \frac{fp - fn}{tp} \quad (7)$$

The boundary distance was measured by computing the minimum distance between manually marked ground truth boundary and the automatically segmented boundary. For a voxel  $(mx_i, my_i, mz_i)$  in the manually marked image, its minimum distance to the automated boundary is defined in equation 8, in which  $(ax_j, ay_j, az_j)$  is a voxel in the automated segmentation.

$$d_i = \arg \min \{ \sqrt{(mx_i - ax_j)^2 + (my_i - ay_j)^2 + (mz_i - az_j)^2} \} \quad (8)$$

#### IV. RESULTS

##### A. Qualitative Evaluation

From the visual inspection of all 339 test cases, the seed point was correctly identified in all cases. For 7.7% cases the second stage failed to trace the ascending aorta all the way to the heart and in 2.3% cases there were surface location errors from stage 3 of the algorithm in the ascending aorta near the surface of the heart. The remaining 305 cases (90%) had very good results. Figure 7 shows 3D visualization of correctly segmented aorta from two different cases as well as an inaccurate case where the ascending aorta was not fully traced to the heart region.



**Fig. 7.** 3D visualization of correctly segmented (left and middle) aorta and an aorta from a case in which tracking terminated early (right).

##### B. Quantitative Evaluation

Table 1 shows a summary of the quantitative evaluation results for all 60 cases. For each case, Dice Similarity Coefficient (DSC), mean boundary distance  $\mu_D$  and the bias term  $B_{pn}$  were computed based on an average over the image slices that have been manually marked. Then for all 60 cases, the mean, standard deviation, maximum and minimum DSC,  $B_{pn}$  and  $\mu_D$  were given in table 1.

Statistics	DSC (Aorta)	DSC(A)	DSC (D)	DSC(Arch)	$B_{pn}$	$\mu_D$ (Aorta)	$\mu_D$ (A)	$\mu_D$ (D)	$\mu_D$ (Arch)
Mean	0.933	0.936	0.939	0.915	0.018	1.39	1.63	1.20	1.42
$\sigma$	0.014	0.019	0.020	0.022	0.054	0.19	0.33	0.29	0.22
Max	0.963	0.972	0.973	0.955	0.123	1.79	2.68	1.96	1.95
Min	0.907	0.889	0.881	0.863	-0.086	0.83	0.69	0.57	0.98

Table 1 Quantitative evaluation results: Average Dice Similarity Coefficients (DSC), bias  $B_{pn}$ , mean boundary distance  $\mu_D$  (mm) and their respective standard deviation  $\sigma$  are given for all 60 cases. Aorta refers to the entire aorta, A refers to ascending aorta, D refers to descending aorta and Arch refers to aortic arch.

## V. DISCUSSION

In most cases (90%) the algorithm provided a high quality segmentation of the aorta in low-dose thin-slice chest CT images. The problems for the algorithm are associated with the ascending aorta near the surface of the heart (10%) and caused by confusion between the aorta and adjacent vessels such as pulmonary trunk and superior vena cava.

Inspection of table 1 shows that for the 60 quantitatively evaluated cases the average DSC is has a high value of 0.933 with a maximum of 0.963 and a minimum of 0.907. The average distance from manually marked boundary to automatically segmented boundary is 1.39mm with a maximum of 1.79mm and a minimum of 0.83mm. Considering that the normal diameter for aorta is typically between 30mm to 40mm, the algorithm has performed an accurate segmentation. It is also observed from table 1  $B_{pn}$  that the algorithm is slightly biased towards over-segmentation. This is due to the fact that variation of intensity values inside the aortic lumen is very small and the fact that aorta is usually surrounded by tissues with similar (for example, heart) or less density values (for example, fat tissue).

While the average DSC and distance measurement is similar across all evaluated cases, some slices have a larger boundary distance ( $>4$ mm). Figure 8(a) and 8(b) illustrate two image slices with small boundary distance while 8(c), 8(d) and 8(e) show slices with very poor boundary distance. Table 2 shows the DSC and maximum boundary distance respectively for the examples in Figure 8. This is usually caused by the unsuccessful termination of rays in stage 3. An inaccurate boundary might occur if step 2 and 3 of the ray termination algorithm (Section II-C) cannot terminate a ray. For all scans, about 8% of the rays cannot be terminated using step 2 or 3. It happens less than 1% of the time for descending aorta region and 10%-15% of the time for ascending aorta region adjacent to other vessels, i.e. for ascending region usually 2 or 3 out of 24 rays fail to terminate per ring of triangles. For such a ray step 4 was used to determine its length based on its closest neighboring rays.

In comparison to other studies, Kurkure et al [5] achieved a DSC of 0.88 in the ascending aorta and 0.96 in the descending aorta compared to 0.94 and 0.94 for this algorithm. Isgum [6] reported a Jaccard coefficient of 0.78 and for this algorithm the corresponding Jaccard coefficient is 0.88. Both comparisons are made on different data sets, with this algorithm being evaluated on significantly more cases, and are therefore limited in interpretation.

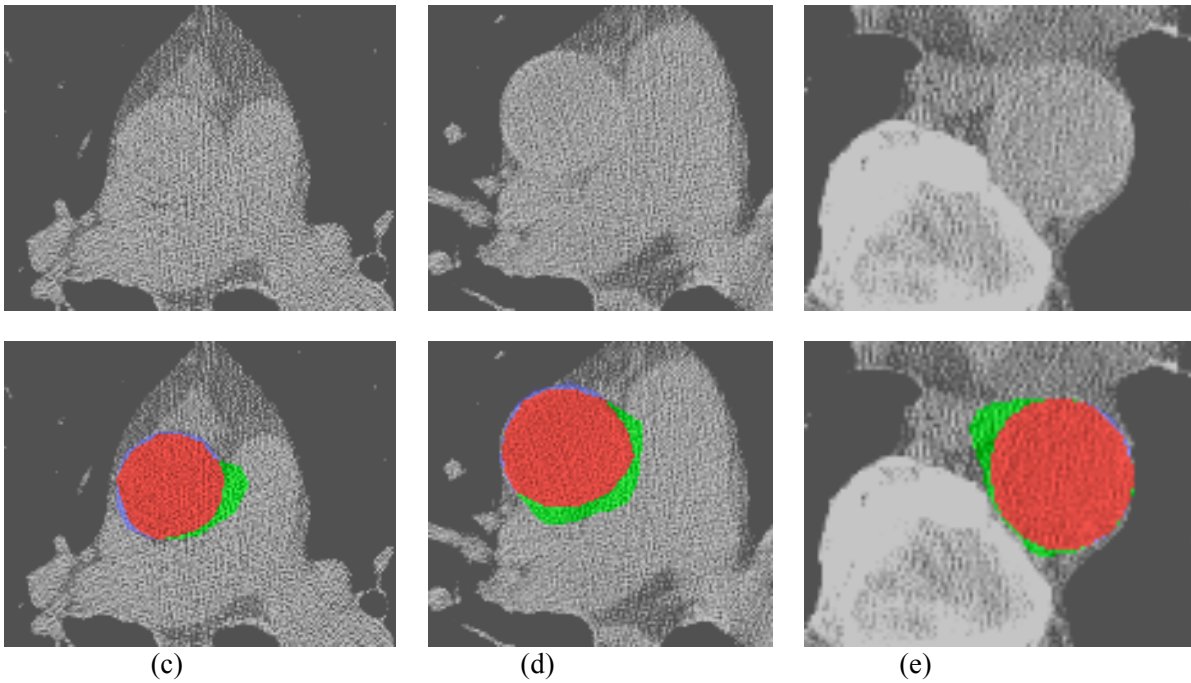
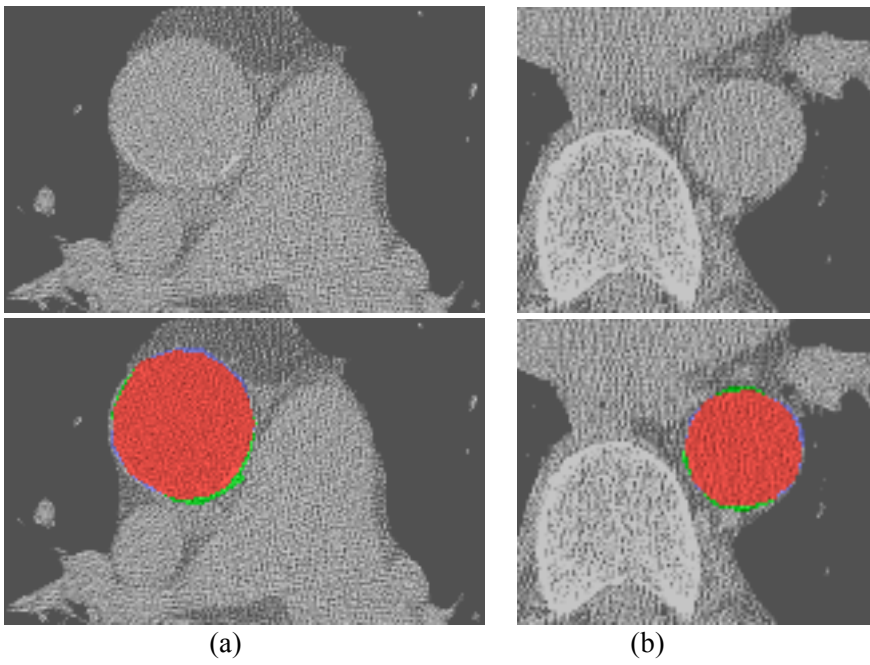


**Fig. 8.** Upper images are original intensity images while corresponding lower images are manually segmented aorta v.s. automatically segmented aorta. Red denotes the overlapping region, green denotes the false positive region and blue denotes the false negative region.

	a	b	c	d	e
DSC	0.962	0.957	0.888	0.877	0.923
Max Distance (mm)	2.39	1.88	4.03	4.01	4.31
Mean Distance(mm)	1.23	1.08	1.89	2.13	1.44

Table 2 Dice Similarity Coefficient, maximum boundary distance and mean boundary distance are given for each of the example slices in Figure8 (a), (b), (c), (d) and (e).

## CONCLUSION

A fully automated aorta segmentation algorithm has been developed for low-dose non-contrast chest CT scans and evaluated using 359 full chest images from VIA-ELCAP and LIDC databases. It employs a cylinder model for approximate aorta location and a surface directed projection model to obtain a valid estimate of the aortic surface location.

The algorithm successfully segmented the aorta in all cases. By visual inspection, about 90% of the cases were successfully segmented. In the other 10% of the cases inaccurate segmentation occurred in heart regions where the aorta is adjacent to organs with similar intensity values. Future work will address this by identifying all vessels in this region. In the quantitative evaluation, the algorithm achieved an average DSC of 0.933 for entire aortic segmentation and an average DSC of 0.936, 0.939 and 0.915 for ascending, descending, and aortic arch segmentation respectively. The average distance was 1.39mm for entire aorta, 1.63mm for ascending aorta, 1.20mm for descending aorta and 1.42mm for aortic arch. Both qualitative and quantitative evaluations indicate that the automated algorithm is able to robustly and accurately segment the aorta in low-dose non-contrast CT scans.

## Statement

Yiting Xie, Jennifer Padgett, and Alberto Biancardi declare that they have no conflict of interest.

Anthony Reeves financial and research disclosures:

Financial:

1. VisionGate, Inc.: Dr. Reeves is a paid consultant and holds stock in the company. VisionGate is developing optical imaging technology for the analysis of individual cells.
2. General Electric: Dr. Reeves is a co-inventor on a patent and other pending patents owned by Cornell Research Foundation (CRF) which are non-exclusively licensed and related to technology involving computer-aided diagnostic methods, including measurement of pulmonary nodules in CT images.
3. D4Vision Inc.: Dr. Reeves is the owner of D4Vision Inc. a company that licenses software for image analysis.

Dr. Reeves receives research support in the form of grants and contracts from: NCI, American Legacy Foundation, Flight Attendants' Medical Research Institute, AstraZeneca, Inc., GlaxoSmithKline and Carestream Health Inc.

All the image data was de-identified and from public databases therefore approval by an ethics committee was not applicable.

## REFERENCES

- [1] S. Schwartz, M. Taljanovic, S. Smyth, M. O'Brien and L. Rogers, "CT Findings of Rupture, Impending Rupture, and Contained Rupture of Abdominal Aortic Aneurysms," *American Journal of Roentgenology*, vol. 188, no. 1, pp. 57-62, 2007.
- [2] S. Hu, E. A. Hoffman and J. M. Reinhardt, "Automatic Lung Segmentation For Accurate Quantitation of Volumetric X-ray CT Images," *IEEE Transactions on Medical Imaging*, vol. 20, pp. 490-498, 2001.
- [3] E. Schwartz, R. Gottardi, J. Holfeld, C. Loewe, M. Czerny and G. Lings, "Evaluating Deformation Patterns of the Thoracic Aorta in Gated CTA Sequences," *ISBI*, pp. 21-24, 2010.
- [4] S. Wang, L. Fu, Y. Yue, Y. Kang and J. Liu, "Fast and Automatic Segmentation of Ascending Aorta in MSCT Volume Data," *CISP*, pp. 1-5, 2009.

- [5] U. Kurkure, O. C. Avila-Montes, and I. A. Kakadiaris, "Automated Segmentation of Thoracic Aorta in Non-contrast CT Images," ISBI, pp. 29–32, 2008.
- [6] I. Isgum, M. Staring, A. Rutten, M. Prokop, M. A. Viergever and B. van Ginneken, "Multi-Atlas-Based Segmentation With Local Decision Fusion-Application to Cardiac and Aortic Segmentation in CT Scans," IEEE Transactions on Medical Imaging, vol. 28, pp.1000–1010, 2009.
- [7] V. Naranjo, J. Angulo, E. Villanueva, M. Alcaniz and S. Lopez-Celdada, "Aorta Segmentation Using the Watershed Algorithm for an Augmented Reality System in Laparoscopic Surgery," ICIP, pp. 2649-2652, 2011.
- [8] P. Burger, S. M. Forbat, R. D. Mohiaddin and G. Z. Yang, "Automatic Tracking of the Aorta in Cardiovascular MR Images Using Deformable Models," IEEE Transactions on Medical Imaging, vol. 16, pp. 581-590, 1997.
- [9] A. O. Al-Agamy, N. F. Osman and A. S. Fahmy, "Segmentation of Ascending and Descending Aorta From Magnetic Resonance Flow Images," 5th CIBEC, pp. 41-44, 2010.
- [10] A. B. De Gonzalez and S. Darby, "Risk of Cancer From Diagnostic X-rays: Estimates for the UK and 14 Other Countries," Lancet, vol. 363, no. 9406, pp. 345-351, 2004.
- [11] A. P. Reeves, A. M. Biancardi, D. F. Yankelevitz, M. D. Cham and C. I. Henschke, "Heart Region Segmentation From Low-dose CT Scans: an Anatomy Based Approach," SPIE International Symposium on Medical Imaging, pp. 83142A, 2012.
- [12] "ELCAP Public Lung Image Database", <http://www.via.cornell.edu/databases/lungdb.html>.
- [13] S. G. Armato et al, "The Lung Image Database Consortium (LIDC) and Image Database Resource Initiative (IDRI): A Completed Reference Database of Lung Nodules on CT Scans," Medical Physics, vol. 38, pp. 915-931, 2011.
- [14] J. Lee and A. P. Reeves, "Segmentation of the Airway Tree From Chest CT Using Local Volume of Interest," 2nd Intl. Workshop of Pulmonary Image Analysis, pp. 333-340, 2009.
- [15] J. Wala, "Automated Pulmonary Artery Segmentation by Vessel Tracking in Low-dose Computed Tomography Images," Masters Dissertation, Cornell University, Ithaca, New York, 2011.
- [16] J. Lee, A. P. Reeves, S. Fotin, T. Apanasovich and D. Yankelevitz, "Human Airway Measurement From CT Images," SPIE International Symposium on Medical Imaging, pp. 691518, 2008.
- [17] S. V. Fotin, A. P. Reeves, M. D. Cham, D. F. Yankelevitz and C. I. Henschke, "Segmentation of Coronary Arteries From CT Angiography Images," SPIE International Symposium on Medical Imaging, pp. 651418, 2007.
- [18] B. Keller, A. P. Reeves, M. D. Cham, C. I. Henschke, and D. F. Yankelevitz, "Semi-Automated Location Identification of Catheters in Digital Chest Radiographs," SPIE International Symposium on Medical Imaging, pp. 651410, 2007.
- [19] J. Lee and A. P. Reeves, "Segmentation of Individual Ribs From Low-dose Chest CT," SPIE International Symposium on Medical Imaging, pp. 76243J, 2010.